Please cite this article in press as: Greene and Shiferaw, A structure-based computational model of IP_3R1 incorporating Ca and IP3 regulation, Biophysical Journal (2024), https://doi.org/10.1016/j.bpj.2024.04.014

Biophysical Journal
Article

Biophysical Society

A structure-based computational model of IP_3R1 incorporating Ca and IP3 regulation

D'Artagnan Greene[1] and Yohannes Shiferaw[1,*]
[1]Department of Physics & Astronomy, California State University, Northridge, California

ABSTRACT The inositol 1,4,5-triphosphate receptor (IP_3R) mediates Ca release in many cell types and is pivotal to a wide range of cellular processes. High-resolution cryoelectron microscopy studies have provided new structural details of IP_3R type 1 (IP_3R1), showing that channel function is determined by the movement of various domains within and between each of its four subunits. Channel properties are regulated by ligands, such as Ca and IP3, which bind at specific sites and control the interactions between these domains. However, it is not known how the various ligand-binding sites on IP_3R1 interact to control the opening of the channel. In this study, we present a coarse-grained model of IP_3R1 that accounts for the channel architecture and the location of specific Ca- and IP3-binding sites. This computational model accounts for the domain-domain interactions within and between the four subunits that form IP_3R1, and it also describes how ligand binding regulates these interactions. Using a kinetic model, we explore how two Ca-binding sites on the cytosolic side of the channel interact with the IP3-binding site to regulate the channel open probability. Our primary finding is that the bell-shaped open probability of IP_3R1 provides constraints on the relative strength of these regulatory binding sites. In particular, we argue that a specific Ca-binding site, whose function has not yet been established, is very likely a channel antagonist. Additionally, we apply our model to show that domain-domain interactions between neighboring subunits exert control over channel cooperativity and dictate the nonlinear response of the channel to Ca concentration. This suggests that specific domain-domain interactions play a pivotal role in maintaining the channel's stability, and a disruption of these interactions may underlie disease states associated with Ca dysregulation.

SIGNIFICANCE This study offers new insights on IP_3R, a key player in sub-cellular Ca release. Utilizing structure-based computational modeling, we show how ligand binding and domain interactions influence the behavior of IP_3R. In particular, we analyze how the two Ca-binding sites and one IP3-binding site interact on the cytosolic side of the channel. These findings may inform future studies on diseases linked to Ca dysregulation due to mutations that affect Ca or IP3 binding to IP_3R, and the model framework that we have developed here can be readily extended to include additional regulatory ligands or different channel types with different regulatory strategies.

INTRODUCTION

The ryanodine receptor (RyR) and the inositol 1,4,5-trisphosphate receptor (IP_3R) are both large tetrameric channels that are essential in regulating calcium (Ca) flow across a variety of cell types (1–4). Presently, there are three known variants of each receptor type. For RyR, these are RyR1, RyR2, and RyR3; for IP_3R, the variants are IP_3R1, IP_3R2, and IP_3R3. Each variant is specific to certain tissue types and plays a critical role in a broad range of cellular functions. In heart cells, RyR2 is responsible for the majority of Ca release from the sarcoplasmic reticulum, whereas the different variants of IP_3R serve to modulate and fine-tune Ca release in response to various signaling pathways (5). Ca release between IP_3Rs and RyRs are tightly coupled because these channels are colocalized, so that Ca release from one channel can diffuse and activate the other (6). Several studies have demonstrated that Ca homeostasis in heart and neural cells is tightly regulated by the crosstalk between these channels. The IP_3R is controlled by Ca and various ligands, mainly inositol 1,4,5-trisphosphate (IP3), which is regulated by the autonomic nervous system. For instance, IP_3Rs in the sinoatrial node are thought to play a significant role in regulating heart rate in response to adrenergic stimulation (7). Also, recent studies have shown that, in diseased conditions such as heart failure, the expression of IP_3Rs is upregulated, and these channels can have an increasingly prominent role in Ca release (8). Consequently, IP_3Rs have been implicated as a possible

Submitted January 5, 2024, and accepted for publication April 12, 2024.
*Correspondence: yshiferaw@csun.edu
Editor: Diego Ferreiro.
https://doi.org/10.1016/j.bpj.2024.04.014

Please cite this article in press as: Greene and Shiferaw, A structure-based computational model of IP_3R1 incorporating Ca and IP3 regulation, Biophysical Journal (2024), https://doi.org/10.1016/j.bpj.2024.04.014

cause of Ca dysregulation leading to various Ca-related cardiac arrhythmias (4).

Recently, researchers have made significant strides in understanding the structure of IP_3R using cryoelectron microscopy (cryo-EM) (9). In particular, a number of recent studies have utilized this technique to identify the location of several key ligand-binding sites within the channel (10–14). One key observation from this work is that both IP3 and Ca-binding sites are located at an interface between structural domains within the channel. This suggests that ligand binding plays a crucial role in controlling the relative motion of domains, which in turn regulates the opening of the channel pore. Furthermore, these studies, and others (10,12), found that several of these binding sites are located at the interface between neighboring subunits, indicating that ligand binding constrains the relative motion of domains between subunits. This finding is consistent with a study where the authors tested an IP_3R channel that contained only three out of four functioning IP3-binding sites. The authors found the channel to be nonfunctional under a wide range of activating concentrations. This result suggested that IP3 needs to bind to all four subunits to activate the channel, and this in turn suggests that the opening of IP_3R is a highly cooperative process (15). Taken together, these results highlight the important role that ligand binding plays in regulating the cooperativity between IP_3R subunits, and this provides new insights into the mechanisms underlying channel activation and inactivation.

IP_3Rs have been studied extensively and there are several mathematical models developed to describe the channel activity (16–20). However, a major limitation of these models is that they do not account for the spatial architecture of the channel. In particular, these models do not incorporate the molecular interactions between domains within the four subunits that regulate the opening and closing of the channel pore. Thus, these models cannot describe channel properties that rely on cooperativity, which is a crucial component of channel regulation (21–24). In this paper, we introduce a coarse-grained model of IP_3R1 that considers the cooperative interactions between domains within the four subunits that form the channel. Specifically, we base our model on data obtained from the recent cryo-EM structures of the closed and open states of the IP_3R1 receptor (11). These studies have pinpointed the locations of two Ca-binding sites and one IP3-binding site on the cytosolic side of the channel, which play a key role in the response of the channel to changes in the concentrations of IP3 and Ca in the cytosol. One of these Ca-binding sites had not been previously identified, and it is unclear how this site can modulate the Ca dependence of the channel. Furthermore, the IP_3R1 current is known to have a bell-shaped dependence on the Ca concentration, and it is not understood how the multiple ligand-binding sites determine this response (25). Thus, our computational model will explore how the key channel properties depend on the detailed architecture of the channel. Based on our analysis, we argue that the newly identified Ca-binding site is likely to be inhibitory at large Ca concentrations to account for the bell-shaped Ca concentration dependence of the IP_3R1 open probability. Our model also provides a new framework to understand how interactions between domains within, and between, subunits contribute to the regulation of the IP_3R1 channel pore. This work provides insights on the stability of IP_3R1 at high and low Ca concentrations and may have implications for Ca dysregulation that underlies various disease states.

MATERIALS AND METHODS

The structure of IP_3R1

The IP_3R is a large transmembrane protein complex composed of four subunits that assemble together side by side to form a central ion pore. Recent cryo-EM studies have yielded structures of the channel with resolutions between 3 and 4 Å (10–14). These studies reveal that each subunit is composed of various domains, and interactions between these domains govern their motion, which controls the opening of the pore. In this study, we analyzed the closed state (PDB: 8EAQ) and open state (PDB: 8EAR) cryo-EM structures of IP_3R1, recently obtained by Fan et al. (11). The Chimera X software (26) was used to identify the domain-domain hydrogen bond (H-bond) interactions in the IP_3R cryo-EM structures. The constraints in the software for identifying H-bonds were relaxed to 1 Å and 50° to allow for some degree of conformational flexibility beyond what is observed in the static cryo-EM structure files. These data were used to identify the H-bond network linking intra-subunit and inter-subunit domains within the IP_3R1 channel.

In Fig. 1, we illustrate the network of H-bond interactions for IP_3R1 between intra-subunit domains and also the H-bond interactions between inter-subunit domains. This representation shows that an IP_3R1 subunit can be roughly separated into three distinct regions. First, there is an outer regulatory region at the far cytosolic end of the channel, which is composed of the domains $\beta TF1$ and $\beta TF2$ (green box). These domains form a circular structure on the cytosolic end of the channel, which is referred to as the βTF ring. The subsequent group of domains—ARM1, ARM2, HD, and ARM3—constitutes a large circular arm that connects the cytosolic side of the channel to the central region closer to the pore (tan box). Last, in the transmembrane and luminal side of the channel, the domains CTD, LNK, ILD, and TMD form the structure surrounding the central pore (blue box). IP_3R1 is regulated by a variety of ligands, especially Ca and IP3, which bind to sites located at the interface between domains. In the cytosolic portion of the channel, Ca-I is located at the inter-subunit interface between $\beta TF2$ on one subunit and the neighboring $\beta TF1$ domain. Ca-II is located at the intra-subunit interface between $\beta TF1$ and $\beta TF2$ on the same subunit. The IP3-binding site is located at the intra-subunit interface between $\beta TF2$ and the ARM1 domain on the same subunit. Additionally, there is a third Ca-binding site, Ca-III, that is found at the intra-subunit interface between the ARM3 and LNK domains, which is far from the βTF ring. Lastly, an ATP-binding site is situated at the intra-subunit interface between the LNK and ILD domains. The positioning of these binding sites at domain-domain interfaces suggests that ligands may regulate the relative movement of domains within a subunit and also between neighboring subunits.

Coarse graining the crystal structure of IP_3R1

In this study, we aim to develop a model of IP_3R1 gating by focusing on the essential domains and binding sites that regulate channel opening. Our approach will be to coarse-grain the system into domains, and clusters of these domains, to understand how ligand binding regulates their interaction.

Please cite this article in press as: Greene and Shiferaw, A structure-based computational model of IP_3R1 incorporating Ca and IP3 regulation, Biophysical Journal (2024), https://doi.org/10.1016/j.bpj.2024.04.014

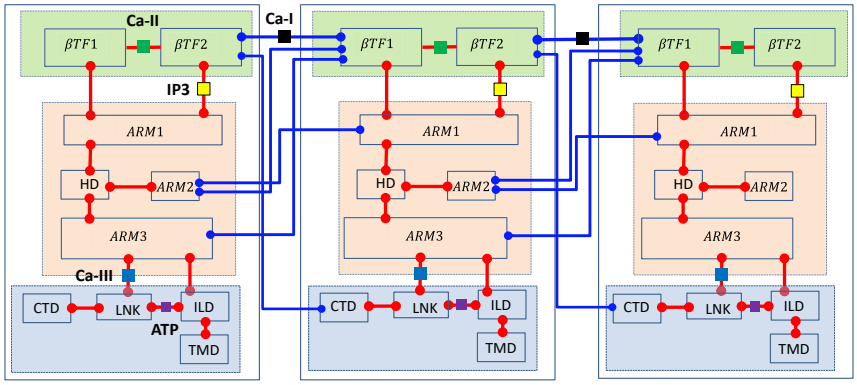

FIGURE 1 The interaction network between the domains that form the subunits of IP_3R1. Each large rectangle corresponds to a subunit and smaller rectangles are the domains within IP_3R1. Links between domains indicate the presence of H-bond interactions between domains. Only the links to the middle subunit are shown. The light green box indicates the *βTF* ring on the cytosolic side of the channel, the tan box the large ring-like structure that connects the regulatory region with the pore, and the set of domains that directly regulate the channel pore (*light blue box*). Regulatory binding sites are Ca-I (*black*), Ca-II (*green*), Ca-III (*blue*), IP3 (*yellow*), and ATP (*purple*). To see this figure in color, go online.

In this approach, each domain will be assigned a time-dependent state variable that is described by a Markovian scheme, with state transitions that are modulated by ligand binding. This phenomenological model is essential since IP_3Rs are among the biggest proteins in biological cells, and it is currently not feasible to simulate the structure-function relationship of the full system. As a starting point, we recognize that the binding sites Ca-I, Ca-II, and IP3 are located at the interface between *βTF*2 and neighboring domains. To capture this structural feature, we will coarse-grain the system as shown in Fig. 2 *A*. Here, we decompose each subunit into the domains *βTF*1, which we designate as *u*, and *βTF*2, which we designate as *v*, and then lump the remaining domains into one region, which we will refer to as the s-region. In Fig. 2 *B*, we show the cryo-EM structure of the IP3R1 channel in the closed state (PDB: 8EAQ) where we have indicated the coarse-grained regions in red (*βTF*1), blue (*βTF*2), and white (s-region), along with the location of the Ca-I-, Ca-II-, and IP3-binding sites on a single subunit. On the right-hand side of Fig. 2 *B*, we show a side view indicating the position of the Ca-III-binding site on a single subunit, which resides in the s-region. We analyzed the cryo-EM structures of Fan et al. (11) using UCSF ChimeraX to count the number of H-bonds between these coarse-grained regions in both the closed (PDB: 8EAQ) and open state (PDB: 8EAR). The results, shown in Table 1, indicate that many H-bonds appear at an interface between neighboring subunits and that there is a surplus of H-bonds in the closed state relative to the open state. Taken together, this suggests that an energy penalty must be overcome to transition from the closed to the open state and that the gating behavior of the channel is likely cooperative.

To model the full channel, we will keep track of the state of each coarse-grained region within the four subunits that make up the channel. To model the state of the *βTF*1 domain we will assign a state vector

$$\vec{u} = (u_1, u_2, u_3, u_4), \qquad \text{(Equation 1)}$$

where u_i will specify the state of *βTF*1 within the i^{th} subunit. Similarly, *βTF*2 will be described using the state vector

$$\vec{v} = (v_1, v_2, v_3, v_4), \qquad \text{(Equation 2)}$$

where v_i represents the state of the i^{th} subunit. The s-region will similarly be described by a state vector

$$\vec{s} = (s_1, s_2, s_3, s_4). \qquad \text{(Equation 3)}$$

To describe ligand regulation, we will keep track of the occupation state of the Ca-I-, Ca-II-, and IP3-binding sites. Thus, for ligand *X* we will assign a vector

$$\vec{n}_X = (n_{X1}, n_{X2}, n_{X3}, n_{X4}), \qquad \text{(Equation 4)}$$

where the component $n_{Xi} = 1$ or 0 if that site is occupied by a ligand or not. In this study, we will denote the four component vectors $\vec{n}_I, \vec{n}_{II}$, and $\vec{n}_{IP3}$ to describe the occupation of the Ca-I-, Ca-II-, and IP3-binding sites, respectively.

Markovian state model of the coarse-grained system

To model the dynamics of the system, we will assign states and transition rates for each coarse-grained region of the subunit. To model the kinetics of *βTF*1 and *βTF*2, we will rely on cryo-EM images showing that these domains shift between two distinct conformations as the channel transitions from the closed to the open state. Thus, we will describe these domains using a simple two-state model (Fig. 2 *C*), where each domain can transition between state 0 and 1. To model the s-region, we will follow the approach of Bicknell et al. (16), who developed a Markovian model of each subunit of an IP_3R tetramer. Our approach will be to apply this Markovian approach to model the s-region in isolation, and then include interactions with neighboring domains. A key feature of the Bicknell model is that it reproduced several essential characteristics of the IP_3R1 current measurements made in lipid bilayers (25,27). In particular, a known property of IP_3R is that it exhibits modal gating where the current switches between three distinct modes of gating activity. To explain modal gating, Bicknell et al. (16) introduced a nonconducting sequestered state and proposed that three or more subunits must be in the open state for channel opening to occur. This simple model naturally partitions the state space of the channel into three distinct regimes that correspond to the observed gating modes. To incorporate these findings, we will apply the four-state Markovian scheme, shown in Fig. 2 *D*, to describe the conformational changes of the group of domains in region-s. The closed IP_3R1 subunit with no Ca bound to the Ca-III-binding site will be represented by state 1. This corresponds to the closed apo-IP_3R1 state when all four subunits are in state 1. It is now well established that Ca-III is the primary Ca-activating site (28) and, upon Ca binding, the subunit can transition to the state 2. Once this transition has occurred, the subunit can either transition to the open state 3, or alternatively transition to a closed conformation 4. These transitions are mediated by interactions between domains, such as the LNK domain, and the s6 segment of the pore. Following the arguments of Bicknell et al., it is this closed sequestered state that is primarily responsible for modal gating. Here, we point out that, as more structural features of IP_3R1 become known, additional states can eventually be included to describe these coarse-grained regions. However, in this study, we have opted for a minimal approach and included only those states that were deemed essential to describe the key experimentally observed channel properties.

Analysis of ligand regulation of an interface

The Ca-I-, Ca-II-, and IP3-binding sites are located at the interface between domains. Thus, ligand binding controls the movement of these domains relative to each other and, as a result, regulates the channel open probability. To model this process, we will first construct a simple model of two

Please cite this article in press as: Greene and Shiferaw, A structure-based computational model of IP$_3$R1 incorporating Ca and IP3 regulation, Biophysical Journal (2024), https://doi.org/10.1016/j.bpj.2024.04.014

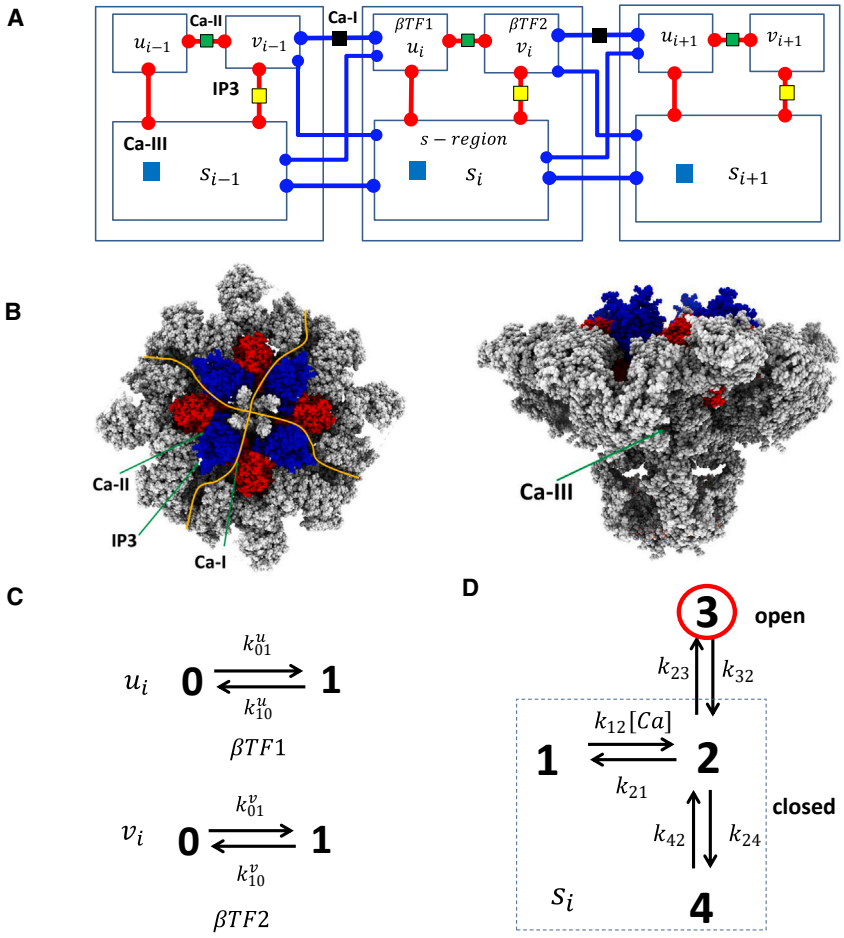

FIGURE 2 Structure based model of IP3R1. (*A*) Coarse-grained model of IP$_3$R1. The $\beta TF1$ domain is described by a variable u_i and $\beta TF2$ is described by a variable v_i, where i denotes the subunit. The s-region is the collection of domains that excludes $\beta TF1$ and $\beta TF2$ and is described by a variable s_i. The blue lines indicate the presence of H-bond interactions between the coarse-grained regions. The Ca-I-binding site is denoted as a black square, the Ca-II-binding site as a green square, the Ca-III-binding site as a blue square, and the IP3-binding site as the yellow square. (*B*) A top view (*left*) of the cryo-EM structure of IP$_3$R1 in the closed state (PDB: 8EAQ) showing the coarse-grained regions $\beta TF1$ (*red*), $\beta TF2$ (*blue*), and the s-region (*white*). The location of the Ca-I-, Ca-II-, and IP3-binding sites for a single subunit are indicated. The orange lines demarcate the boundary between subunits. A side view (*right*) of the cryo-EM structure of IP3R1 in the closed state showing the location of the Ca-III-binding site for a single subunit. (*C*) Transition rates of the $\beta TF1$ and $\beta TF2$ domains. (*D*) Markov state diagram and transition rates describing the s-region. To see this figure in color, go online.

domains that interact in a ligand-dependent manner. Once this model is developed, we will then apply the formalism to all interfaces in our coarse-grained model of IP$_3$R1. A simple two-domain system is illustrated in Fig. 3 *A*, which consists of domain x and y. In isolation, domains x and y can attain states 0 or 1 according to the reaction scheme shown in Fig. 3 *B*. Here, we will place the binding site on domain x, which can either be occupied ($n = 1$) or unoccupied ($n = 0$). Finally, we will assume that, if $x = 1$ and $y = 1$, a binding pocket is formed at the interface and ligand binding will render that conformation more energetically stable. Here, the assumption is that, in that conformation, there are local structural rearrangements that form an energetically stable binding pocket (29). The possible states of the system can be labeled as a triplet of numbers $\vec{X} = (x,y,n)$, which yields eight distinct states of the system. To assign energies to these states, we will let the energy of domain x have the form

$$E_x(n,x) = E_x(x) + \epsilon_x \delta_{n,1}, \qquad \text{(Equation 5)}$$

where $E_x(x)$ is the energy of the domain in state x, and ϵ_x is the binding energy of the ligand to domain x. Here, the Kronecker delta symbol is defined so that $\delta_{n,1} = 1$ if $n = 1$ and zero otherwise. Similarly, the energy of domain y will be denoted as $E_y(y)$. To model the interaction between domains, we will take the interface energy to have the form

$$E_{xy}(x,y,n) = E_{xy}(x,y) + \epsilon_{xy}\delta_{n,1}\delta_{x,1}\delta_{y,1}, \qquad \text{(Equation 6)}$$

where $E_{xy}(x,y)$ denotes the total energy of all interactions across the interface between domains x and y, and the last term represents the binding-energy contribution due to the favored conformation with $x = 1$ and $y = 1$. The total energy of the two-domain system will have the form

$$E\left(\vec{X}\right) = E_x(x) + E_y(y) + E_{xy}(x,y) + \epsilon_x\delta_{n,1} + \epsilon_{xy}\delta_{n,1}\delta_{x,1}\delta_{y,1}. \qquad \text{(Equation 7)}$$

Note here that in the conformation $x = 1$ and $y = 1$ the total binding energy is given by the sum $\epsilon_x + \epsilon_{xy}$.

The dynamics of our two-domain system will be dictated by the transition rate between conformational states. The overarching principle

TABLE 1 The Number of H-Bonds Linking the Indicated Coarse-grained Regions in the Closed (PDB: 8EAQ) and open (PDB: 8EAR) Cryo-EM Structures of IP$_3$R1

Coarse-Grained Regions	H-Bonds (Closed)	H-Bonds (Open)
$u_i - v_i$	3	1
$u_i - s_i$	4	4
$v_i - s_i$	2	3
$s_i - s_{i+1}$	36	20
$s_i - u_{i+1}$	16	3
$s_i - v_{i-1}$	5	0

Interactions between β TF1 (u), β TF2 (v), and the s-region are shown between domains on the same subunit (i) or between one subunit (i) and a neighboring subunit ($i+1$). UCSF ChimeraX was used to count the number of H-bonds in both structures. The constraints in the software for identifying H-bonds were relaxed to 1 Å and 50° to allow for some degree of conformational flexibility beyond the static cryo-EM structure files.

Please cite this article in press as: Greene and Shiferaw, A structure-based computational model of IP_3R1 incorporating Ca and IP3 regulation, Biophysical Journal (2024), https://doi.org/10.1016/j.bpj.2024.04.014

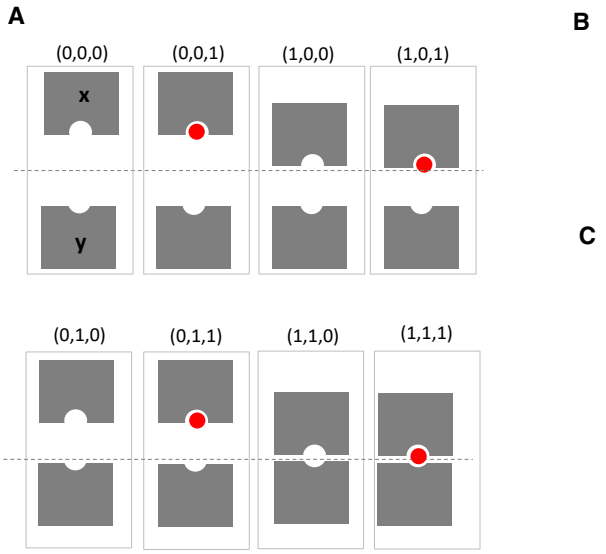

FIGURE 3 A simple model of ligand binding to an interface between two domains. (*A*) Illustration of domain x and y interacting at an interface regulated by a ligand (*red filled circle*) that binds to domain x. Each domain can be in either state 0 (domain away from dashed line) or 1 (close to dashed line). The binding pocket is formed when $x = 1$ and $y = 1$. (*B*) Transition rates of domain x and y in the absence of ligand. (*C*) Ligand-binding reaction rates to domain x. To see this figure in color, go online.

governing these transition rates is that they must satisfy the principle of detailed balance. To apply detailed balance, note that, at equilibrium, the statistical weight of a state $\vec{X}$ is given by

$$W\left[\vec{X}\right] \propto \exp\Big(-\beta\Big[E\left(\vec{X}\right) - \mu n\Big]\Big), \qquad \text{(Equation 8)}$$

where μ is the chemical potential, which is the free energy required to extract the ligand from the surrounding solution. The transition rate between any two states $\vec{X}$ and $\vec{X}'$ should then satisfy the detailed balance condition.

$$\frac{K\left[\vec{X}\to\vec{X}'\right]}{K\left[\vec{X}'\to\vec{X}\right]} = \frac{W\left[\vec{X}'\right]}{W\left[\vec{X}\right]}, \qquad \text{(Equation 9)}$$

where $K[\vec{X}\to\vec{X}']$ denotes the transition rate from state $\vec{X}$ to state $\vec{X}'$.

To model the transition rates between states, we will first consider the case where the domains x and y are in isolation. In this case, detailed balance requires that the transition rates, given in Fig. 3 *B*, satisfy

$$\Delta E_x = -\frac{1}{\beta}\ln\left(\frac{k^x_{01}}{k^x_{10}}\right), \qquad \text{(Equation 10)}$$

$$\Delta E_y = -\frac{1}{\beta}\ln\left(\frac{k^y_{01}}{k^y_{10}}\right), \qquad \text{(Equation 11)}$$

where $\Delta E_x = E_x(1) - E_x(0)$ and $\Delta E_y = E_y(1) - E_y(0)$. Thus, if we set $E_x(0) = E_y(0) = 0$ then $E_x(1)$ and $E_y(1)$ are determined from the detailed balance constraint. If domains x and y interact, then the transition rates will depend on the interface energy between the two domains. Here, we will first consider the case where ligands are absent so that $n = 0$ in Eq. 7. In this case, domain x will transition between state 0 and 1 with a transition rate that satisfies

$$\frac{K[(0,y,0)\to(1,y,0)]}{K[(1,y,0)\to(0,y,0)]} = \exp(-\beta(E_x(1) - E_x(0)))\exp\Big(-\beta\big(E_{xy}(1,y) - E_{xy}(0,y)\big)\Big), \qquad \text{(Equation 12)}$$

which can be simplified to

$$\frac{K[(0,y,0)\to(1,y,0)]}{K[(1,y,0)\to(0,y,0)]} = \frac{k^x_{01}}{k^x_{10}}\exp\big(-\beta\Delta E_{xy}\big), \qquad \text{(Equation 13)}$$

where

$$\Delta E_{xy} = E_{xy}(1,y) - E_{xy}(0,y) \qquad \text{(Equation 14)}$$

is the difference in the interface energy of the two conformations. Note that detailed balance only places a constraint on the ratio of rates and does not specify the particular form of these rates. To implement the detailed balance condition, we will take the forward transition rate to have the form

$$K[(0,y,0)\to(1,y,0)] = k^x_{01}\exp\big(-\beta\eta\Delta E_{xy}\big), \qquad \text{(Equation 15)}$$

where η is a constant parameter that determines the effect of the change in interface energy ΔE_{xy}. Detailed balance requires that the backward rate must then have the form

$$K[(1,y,0)\to(0,y,0)] = k^x_{10}\exp\big(-\beta(\eta - 1)\Delta E_{xy}\big). \qquad \text{(Equation 16)}$$

In this study, we will treat the forward and backward reaction rates on the same footing and take $\eta = 1/2$. In this way, detailed balance is satisfied and the reaction rates k^x_{01} and k^x_{10} are simply modified by an exponential factor that depends only on the interface energy between neighboring coarse-grained regions.

To account for ligand binding, it is necessary to account for the chemical potential of the ligand. Detailed balance requires that the binding reaction rate must satisfy

$$\frac{K[(x,y,0)\to(x,y,1)]}{K[(x,y,1)\to(x,y,0)]} = \exp\big(-\beta\Delta E_{xy}\big)\exp(\beta\mu), \qquad \text{(Equation 17)}$$

where

$$\Delta E_{xy} = E(x,y,1) - E(x,y,0), \qquad \text{(Equation 18)}$$

is the difference in interface energy between the bound and unbound conformation. Using Eq. 7, the energy difference can be written as

$$\Delta E_{xy} = \epsilon_x + \epsilon_{xy}\delta_{x,1}\delta_{y,1}, \qquad \text{(Equation 19)}$$

so that

$$\frac{K[(x,y,0)\to(x,y,1)]}{K[(x,y,1)\to(x,y,0)]} = \exp(-\beta(\epsilon_x - \mu))\exp\big(-\beta\epsilon_{xy}\delta_{x,1}\delta_{y,1}\big). \qquad \text{(Equation 20)}$$

Please cite this article in press as: Greene and Shiferaw, A structure-based computational model of IP_3R1 incorporating Ca and IP3 regulation, Biophysical Journal (2024), https://doi.org/10.1016/j.bpj.2024.04.014

To account for the chemical potential and binding energy prefactor, it is more convenient to use the binding reaction rates given in Fig. 3 *C*. In this approach, the binding rate constants k_+^L and k_-^L are simply related to the binding energy and chemical potential according to

$$\frac{k_+^L[L]}{k_-^L} = \exp(-\beta(\epsilon_x - \mu)). \quad \text{(Equation 21)}$$

Thus, we can write

$$\frac{K[(x,y,0)\to(x,y,1)]}{K[(x,y,1)\to(x,y,0)]} = \frac{k_+^L[L]}{k_-^L}\exp\left(-\beta\epsilon_{xy}\delta_{x,1}\delta_{y,1}\right). \quad \text{(Equation 22)}$$

Treating forward and backward reaction rates on the same footing requires that

$$K[(x,y,0)\to(x,y,1)] = k_+^L[L]\exp\left(-\frac{\beta\epsilon_{xy}}{2}\delta_{x,1}\delta_{y,1}\right), \quad \text{(Equation 23)}$$

and

$$K[(x,y,1)\to(x,y,0)] = k_-^L\exp\left(\frac{\beta\epsilon_{xy}}{2}\delta_{x,1}\delta_{y,1}\right). \quad \text{(Equation 24)}$$

Here, we see that the binding reaction rates are multiplied by an exponential factor that promotes the binding of the ligand to the conformation $x = 1$ and $y = 1$. Using this approach, we can now determine the transition rates between all conformational states of our coarse-grained model of IP_3R1.

The structure of Ca and IP3 regulation of IP_3R1

Our coarse-grained approach simplifies the full IP_3R1 to a system that is specified by six four-component vectors $(\vec{s},\vec{u},\vec{v},\vec{n}_I,\vec{n}_{II},\vec{n}_{IP3})$ with $4^4 2^{4\times 5} = 2^{28}$ distinct states. To determine the transition rates between these states, we will compute the energy of all conformations of the system. To simplify the system further, we will assume that the interface energy between two nearest-neighbor s-regions will depend only on a reduced variable $\tilde{s}_i$ defined as

$$\tilde{s}_i = \begin{cases} 1 & IF \quad s_i = 3 \\ 0 & IF \quad s_i \in 1,2,4 \end{cases}. \quad \text{(Equation 25)}$$

Here, the assumption is that the s-region will change conformation to increase the pore diameter when $s_i = 3$, and that the conformations with $s_i \in 1,2,4$ are roughly the same with respect to a nearest-neighbor subunit. Thus, with regard to the interface energies, we will specify the conformation of each s-region using the variable $\tilde{s}_i$. The interface energy between the s-region in subunit i and neighboring interfaces, and which are also independent of ligand binding, are denoted in Table 2. Here, primed energies are between regions on different subunits, whereas unprimed energies are between domains within the same subunit. Note also that i ranges from 1 to 4 and that we will impose periodic boundary conditions so that, for instance, for the s-region we will set $s_5 = s_1$ and $s_0 = s_4$. To account for interfaces that are regulated by ligand binding, we will apply our two-domain approach to all interfaces of our coarse-grained model.

To determine the binding interactions, we will rely on experimental studies that have established how IP_3R1 responds to changes in Ca and IP3 concentration (25,27). In particular, it is known that, for IP3 concentrations less than $\sim 0.03\mu M$, the channel is effectively shut for all Ca concentrations. Above this threshold, the channel open probability P_o rises substantially to a level that is determined by the cytosolic Ca concentration. Thus, IP3 serves as a potent channel activator. Also, Fan et al. (11) identified the Ca-I-binding site and argued that this site is likely responsible for inactivating the channel at high Ca concentrations. However, this study was inconclusive on how the Ca-II Ca-binding site modulated channel gating. To model ligand regulation of our coarse-grained model, we will describe each interface using the two-state model developed in the previous section. In Fig. 4 *A* we show the network diagram showing the location of the binding sites at the interface between domains. Here, we will assume that Ca and IP3 will bind to the sites Ca-I, Ca-II, and IP3, with reaction rates shown in Fig. 4 *B*. These reactions rates are related to the binding energy and chemical potential according to Eq. 21. In this approach, it is not necessary to specify which domain on the interface the ligand is bound to. To assign binding energies to the energetically favorable conformation, we note that the $\beta TF2$ domain on subunit i, which is represented by the variable v_i, is linked to all ligand-binding sites on the cytosolic side of the channel.

TABLE 2 Ligand-Independent Interaction Energies

Domains	Interface Energy
$s_i - u_i$	$E_{su}(\tilde{s}_i, u_i)$
$s_i - s_{i+1}$	$E'_{ss}(\tilde{s}_i, \tilde{s}_{i+1})$
$s_i - u_{i+1}$	$E'_{su}(\tilde{s}_i, u_{i+1})$
$s_i - v_{i-1}$	$E'_{sv}(\tilde{s}_i, v_{i-1})$

Interface energies between the s-region of subunit i and neighboring domains $\beta TF1$ (u) and $\beta TF2$ (v). Interface energies shown are independent of ligand binding. Unprimed energies are between domains on the same subunit, whereas primed energies are between domains in nearest-neighbor subunits.

In particular we note that 1) IP3 functions as an activator by reinforcing the interaction between the ARM1 domain of the s-region (s_i) and $\beta TF2$ in the same subunit (v_i); 2) Ca binding to Ca-I strengthens the interaction between $\beta TF2$ (v_i) and $\beta TF1$ on the adjacent subunit (u_{i+1}), which promotes channel closure. From these observations, we deduce that the $\beta TF1$ domain is a channel inactivator, since an increase in the interaction with this domain promotes channel closure. Also, $\beta TF2$ must act as an activator since a stronger binding to this domain promotes channel opening. To implement these conditions in a straightforward manner, we will choose model parameters that satisfy the following:

1) $\beta TF2$ resides in the state $v_i = 0$ *or* 1 with equal probability. When $\beta TF2$ is in state $v_i = 1$ and the s-region is in the open state $\tilde{s}_i = 1$, then an IP3-binding pocket is formed. In this manner, IP3 binding to that site will favor subunit opening by stabilizing the $\tilde{s}_i = 1$ state.
2) $\beta TF1$ resides in the state $u_i = 0$ and Ca binding to Ca-I stabilizes the conformation with $v_i = 0$ and $u_{i+1} = 0$. In this manner, Ca binding to Ca-I will stabilize the $v_i = 0$ state of $\beta TF2$ and promote channel closure.

To incorporate these interactions, we will take the interface energy between $\beta TF2$ and $\beta TF1$ on the adjacent subunit to have the form

$$E'_{vu}(v_i, u_{i+1}, n_{Ii}) = E'_{vu}(v_i, u_{i+1}) + \epsilon_I\delta_{v_i,0}\delta_{u_{i+1},0}\delta_{n_{Ii},1}, \quad \text{(Equation 26)}$$

which stabilizes the $v_i = 0$ and $u_{i+1} = 0$ configuration if the Ca-binding energy is $\epsilon_I < 0$. Similarly, we will model binding to IP3 using

$$E_{sv}(s_i, v_i, n_{IP3i}) = E_{sv}(s_i, v_i) + \epsilon_{IP3}\delta_{\tilde{s}_i,1}\delta_{v_i,1}\delta_{n_{IP3i},1}, \quad \text{(Equation 27)}$$

where the binding energy is $\epsilon_{IP3} < 0$, so that IP3 binding will stabilize the open subunit $\tilde{s}_i = 1$ and $v_i = 1$. The states that are favored by ligand binding are illustrated in Fig. 4 *C*. In this manner, IP3 will serve as an activator that will stabilize the open subunit, whereas Ca binding to Ca-I will negate this effect by stabilizing the closed subunit.

To model the effect of Ca-II, we will first consider the case when this binding site is inactivating. In this case, we require that Ca binding to

Please cite this article in press as: Greene and Shiferaw, A structure-based computational model of IP$_3$R1 incorporating Ca and IP3 regulation, Biophysical Journal (2024), https://doi.org/10.1016/j.bpj.2024.04.014

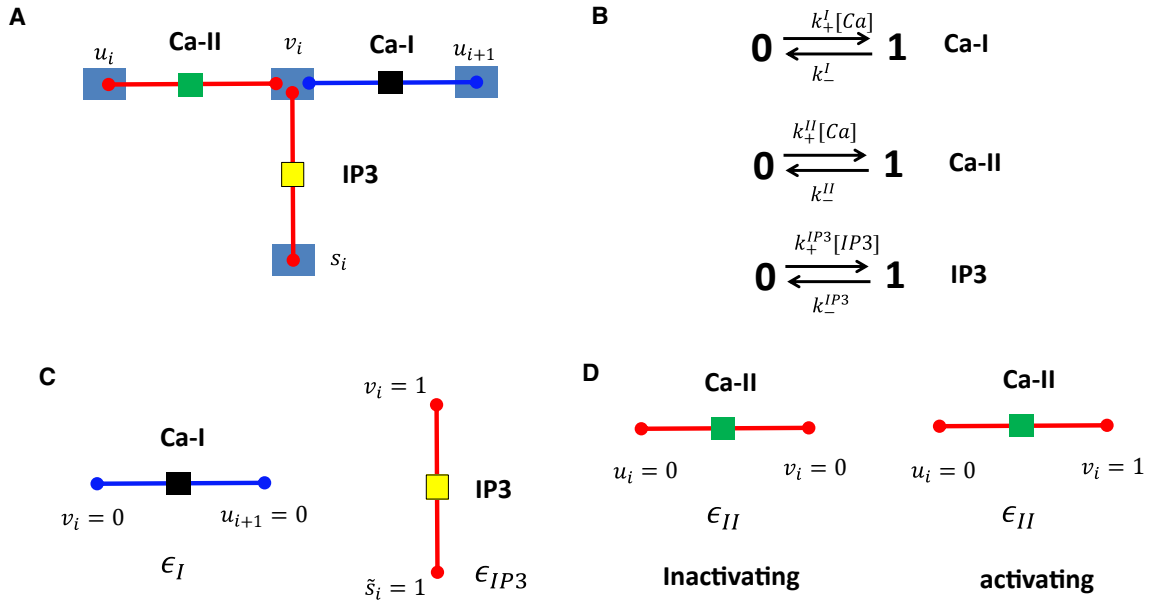

FIGURE 4 Ligand regulation of IP$_3$R1. (*A*) The network of interactions linking the Ca-I-, Ca-II-, and IP3-binding sites to neighboring domains. (*B*) Binding reaction rates at sites Ca-I, Ca-II, and IP3. (*C*) Energetically favored conformations. Ca binding to Ca-I will favor state $v_i = 0$ and $u_{i+1} = 0$ with a binding energy ϵ_I, whereas IP3 binding to the IP3-binding site will favor $v_i = 1$ and $\tilde{s}_i = 1$ with binding energy ϵ_{IP3}. (*D*) Energetically favored states for Ca binding to Ca-II. Left/right configuration is inactivating/activating. To see this figure in color, go online.

Ca-II will strengthen the coupling between $\beta TF1$ and $\beta TF2$ on the same subunit and therefore stabilize the $v_i = 0$ state of $\beta TF2$. This effect will favor the closing of the subunit due to the stronger coupling to the coarse-grained region-s. To implement this effect, we will let the interaction energy between u_i and v_i have the form

$$E_{uv}(u_i, v_i, n_{IIi}) = E_{uv}(u_i, v_i) + \epsilon_{II}\delta_{u_i,0}\delta_{v_i,0}\delta_{n_{IIi},1}. \quad \text{(Equation 28)}$$

On the other hand, if Ca-II is an activating binding site, then Ca binding will favor $v_i = 1$. This can be achieved in the same way by taking

$$E_{uv}(u_i, v_i, n_{IIi}) = E_{uv}(u_i, v_i) + \epsilon_{II}\delta_{u_i,0}\delta_{v_i,1}\delta_{n_{IIi},1} \quad \text{(Equation 29)}$$

so that $v_i = 1$ will be energetically favored by Ca binding. Both of these cases are illustrated in Fig. 4 *D*. In Table 3, we summarize all the interaction energies that are dependent on ligand binding.

Given the interaction energy at all interfaces and their ligand dependence, the total energy of IP$_3$R1 can now be written as

$$E\left[\vec{X}\right] = E_d\left[\vec{X}\right] + E_{nn}\left[\vec{X}\right], \quad \text{(Equation 30)}$$

where

$$E_d\left[\vec{X}\right] = \sum_{i=1}^{4} E_s(s_i) + E_u(u_i) + E_v(v_i) + \epsilon_b^I\delta_{nIi,1} + \epsilon_b^{II}\delta_{nIIi,1} + \epsilon_b^{IP3}\delta_{nIP3i,1} \quad \text{(Equation 31)}$$

is the energy of each domain in isolation, and where the summation is over all four subunits. Here, we include the energy of the s-region ($E_s(s_i)$), the energy of $\beta TF1$ ($E_u(u_i)$), and the energy of $\beta TF2$ ($E_v(v_i)$). To determine these energies, we will first set $E_s(s_i = 1) = 0, E_u(u_i = 0) = 0$ and $E_v(v_i = 0) = 0$, and all other energies for each domain will be determined by the Markov transition rates (see Table 4). The last three terms denote the binding energy to sites Ca-I, Ca-II, and IP3, independently of the conformation of the neighboring domain. The energy due to the interface between regions can be expressed in the form

$$E_{nn}\left[\vec{X}\right] = \sum_{i=1}^{4} E_{su}(\tilde{s}_i, u_i) + E'_{ss}(\tilde{s}_i, \tilde{s}_{i+1}) + E'_{su}(\tilde{s}_i, u_{i+1}) + E'_{sv}(\tilde{s}_i, v_{i-1}) + E_{sv}(\tilde{s}_i, v_i, n_{IP3i}) + E'_{vu}(v_i, u_{i+1}, n_{Ii}) + E_{uv}(u_i, v_i, n_{IIi}) \quad \text{(Equation 32)}$$

TABLE 3 Ligand-Dependent Interaction Energies

Domains	Binding Site	Interface Energy
$v_i - u_{i+1}$	Ca-I	$E'_{vu}(v_i, u_{i+1}, n_{Ii}) = E'_{uv}(v_i, u_{i+1}) + \epsilon_I\delta_{v_i,0}\,\delta_{u_{i+1},0}\,\delta_{n_{Ii},1}$
$s_i - v_i$	IP3	$E_{sv}(s_i, v_i, n_{IP3i}) = E_{sv}(s_i, v_i) + \epsilon_{IP3}\delta_{\tilde{s}_i,1}\delta_{v_i,1}\,\delta_{n_{IP3i},1}$
$u_i - v_i$	Ca-II (inactivating)	$E_{uv}(u_i, v_i, n_{IIi}) = E_{uv}(u_i, v_i) + \epsilon_{II}\,\delta_{u_i,0}\delta_{v_i,0}\delta_{n_{IIi},1}$
$u_i - v_i$	Ca-II (activating)	$E_{uv}(u_i, v_i, n_{IIi}) + E_{uv}(u_i, v_i) + \epsilon_{II}\,\delta_{u_i,0}\delta_{v_i,1}\delta_{n_{IIi},1}$

Interface energies between coarse-grained regions and domains that are regulated by ligand binding.

Please cite this article in press as: Greene and Shiferaw, A structure-based computational model of IP_3R1 incorporating Ca and IP3 regulation, Biophysical Journal (2024), https://doi.org/10.1016/j.bpj.2024.04.014

TABLE 4 Relationship between Energy and Markov Transition Rates for Region-s and $\beta TF2$

Coarse-Grained Region	State	Energy
Region-s	1	$E_s(1) = 0$
Region-s	2	$E_s(2) = -(1/\beta)\ln(k_{12}[Ca]/k_{21})$
Region-s	3	$E_s(3) = -(1/\beta)\ln(k_{23}/k_{32})$
Region-s	4	$E_s(4) = -(1/\beta)\ln(k_{24}/k_{42})$
$\beta TF2$ (v)	0	$E_v(0) = 0$
$\beta TF2$ (v)	1	$E_v(1) = -(1/\beta)\ln(k_v^{01}/k_v^{10})$

where we impose periodic boundary conditions so that $\tilde{s}_5 = \tilde{s}_1, u_5 = u_1, v_0 = v_4$.

The open probability

To evaluate the open probability of IP_3R1, we note that the statistical weight of each configuration can be written as

$$W\left[\vec{X}\right] \propto \exp\Big(-\beta\Big[\tilde{E}\Big(\left[\vec{X}\right]\Big) - \left(\mu_I - \epsilon_b^I\right)m_I - \left(\mu_{II} - \epsilon_b^{II}\right)m_{II} - \left(\mu_{IP3} - \epsilon_b^{IP3}\right)m_{IP3}\Big]\Big), \quad \text{(Equation 33)}$$

where

$$m_I = \sum_{i=1}^{4} n_{Ii}, \quad \text{(Equation 34)}$$

$$m_{II} = \sum_{i=1}^{4} n_{IIi}, \quad \text{(Equation 35)}$$

$$m_{IP3} = \sum_{i=1}^{4} n_{IP3,i}, \quad \text{(Equation 36)}$$

are the number of bound ligands at the Ca-I-, Ca-II-, and IP3-binding sites. Here, the energy $\tilde{E}[\vec{X}]$ is simply the total energy of the system excluding the binding energy contributions due to $\epsilon_b^I, \epsilon_b^{II}$, and ϵ_b^{IP3}. Using Eq. 33, the statistical weight for a given conformation can be written as

$$W\left[\vec{X}\right] \propto \exp\left(-\beta\tilde{E}\left[\vec{X}\right]\right)(K_I[Ca])^{m_I}(K_{II}[Ca])^{m_{II}}(K_{IP3}[IP3])^{m_{IP3}}, \quad \text{(Equation 37)}$$

where the association constants for each binding site have the form $K_X = k_X^+/k_X^-$, where X denotes the binding site in question.

To compute the equilibrium open probability of the IP_3R channel, we will first compute the number of open subunits for each configuration denoted as

$$n_o = \sum_{k=1,4} \delta_{\tilde{s}_k,1}. \quad \text{(Equation 38)}$$

We will follow Bicknell et al. (16) and posit that the full channel is open providing $n_0 \geq 3$, which gives an open probability

$$\frac{\sum_{\vec{X},n_o \geq 3} W\left[\vec{X}\right]}{\sum_{\vec{X}} W\left[\vec{X}\right]}, \quad \text{(Equation 39)}$$

where the numerator is summed only over all states with $n_0 \geq 3$.

Dynamics and numerical simulations

To construct thermodynamically consistent transition rates for the full IP_3R1, we will apply our analysis of the simplified two-domain model. As a starting point, we will first consider the transition rates between states at fixed ligand number. In this case, for a domain, subunit i, in state x_i to transition to x_i' we will apply a transition rate

$$K\left[\ldots, x_i, \ldots \rightarrow \ldots x_i', \ldots\right] = k\left(x_i \rightarrow x_i'\right)\exp\left(-\beta\frac{\Delta E_{nn}}{2}\right), \quad \text{(Equation 40)}$$

where

$$\Delta E_{nn} = \Delta E_{nn}\left[\ldots, x_i', \ldots\right] - E_{nn}[\ldots, x_i, \ldots], \quad \text{(Equation 41)}$$

is the energy difference between the initial and final states, and where $k(x_i \rightarrow x_i')$ is the transition rate for that domain in the absence of nearest-neighbor coupling. For binding reactions for ligand L to binding site X on subunit i, the binding rate will be

$$K[\ldots, n_{Xi} = 0, \ldots \rightarrow \ldots, n_{Xi} = 1, \ldots] = k_X^+[L]\exp\left(-\beta\frac{\Delta E_{nn}}{2}\right), \quad \text{(Equation 42)}$$

where

$$\Delta E_{nn} = E_{nn}[\ldots, n_{Xi} = 1, \ldots] - E_{nn}[\ldots, n_{Xi} = 0, \ldots]. \quad \text{(Equation 43)}$$

Here, k_x^+ will denote the binding rate to site X independently of nearest-neighbor coupling. Similarly, the unbinding rate will have the form

$$K[\ldots, n_{Xi} = 1, \ldots \rightarrow \ldots, n_{Xi} = 0, \ldots] = k_X^-\exp\left(-\beta\frac{\Delta E_{nn}}{2}\right), \quad \text{(Equation 44)}$$

where

$$\Delta E_{nn} = E_{nn}[\ldots, n_{Xi} = 0, \ldots] - E_{nn}[\ldots, n_{Xi} = 1, \ldots]. \quad \text{(Equation 45)}$$

Numerical simulations

To model the dynamics of IP_3R1, we will apply the standard Gilespie algorithm (30) to simulate the exact stochastic evolution of the coarse-grained model. In this approach, the system is initialized in state $\vec{X}(t)$ at time t, and the time of the next reaction is taken from an exponential distribution $P(\tau) = k_o\exp(-k_o\tau)$, where $k_o = \sum k_j$ is the sum over all the reaction rates in the system. Once the next reaction time is determined, then reaction j will occur with probability k_j/k_o. Our coarse-grained model can be simulated by applying this algorithm to the 28 possible reactions that can occur at each time step.

RESULTS

Kinetics and equilibrium of IP_3R1

In this section, we will apply our coarse-grained model to fit experimental data derived from IP_3R current recordings.

Please cite this article in press as: Greene and Shiferaw, A structure-based computational model of IP_3R1 incorporating Ca and IP3 regulation, Biophysical Journal (2024), https://doi.org/10.1016/j.bpj.2024.04.014

Although this study will not focus on extensive model fitting, it will provide a means to evaluate how well the architecture of our coarse-grained model aligns with the available experimental data. Our analysis will be based on experimental studies of Ionescu et al. (25), who measured single-channel IP_3R currents in *Spodoptera frugiperda* (Sf9) cells. In this study, they measured the mean open probability (P_o), the average closed time (τ_c), and the open time (τ_o) as a function of Ca and IP3 concentration. To find model parameters, we build on the work of Bicknell et al. (16), who developed a four-subunit model of IP_3R, where each subunit was independent and described using a Markovian state model. The parameters were manually adjusted to visually fit the data, which was deemed appropriate for the level of detail required for the present analysis. To model the kinetics of the $\beta TF2$ domain, we will set $k_v^{01} = k_v^{10} = 0.1\ (ms)^{-1}$ so that this domain is neutral in the absence of nearest-neighbor coupling. Model parameters describing the transition rates of the s-region and the βTF2 domain are given in Table 5, and the binding transition rates are shown in Table 6. To account for the energy changes at the interface between domains, we will first consider the cases that are independent of ligand binding. Here, we will rely on our H-bond analysis (Table 1), which reveals an extensive H-bond network between domains in both the closed- and open-state structures. The ability to form such H-bonds is dependent on both the conformation of a domain and the conformation of a neighboring domain. Thus, we must include an energy penalty for domains that are in mismatched conformational states. To accomplish this, we set all ligand-independent interface energies, between domains x and y, to have the form $\beta E_{xy}(0,0) = -\delta$ and $\beta E_{xy}(1,1) = -\delta$, $\beta E_{xy}(0,1) = \beta E_{xy}(1,0) = \delta$. Here, the parameter $\delta > 0$ denotes the strength of the interaction that favors alignment between nearest neighbors, i.e., the conformations (0,0) and (1,1), and that penalizes a state mismatch, i.e., (0,1) or (1,0). In this study we found that taking $\delta = 0.3$ for all interfaces in the coarse-grained model was sufficient to fit the experimental data. The selection of this parameter ensured that cooperative interactions between nearest neighbors modulated transition rates by a factor $\sim \exp(\delta) \approx 1.3$, which introduced some degree of cooperativity but was not large enough to dictate the overall kinetics of the channel. Here, we note that we have simplified the system by treating all interfaces on the same footing. For our present analysis, this was necessary since, if each interface was assigned a different energy, it would lead to a substantial expansion of the parameter space, which cannot be constrained by the available experimental data.

TABLE 5 Transition Rates for the s-Region and the $\beta TF2$ Domain

Transition Rate	Value
k_{12}	$0.040\ (ms)^{-1}(\mu M)^{-1}$
k_{21}	$0.010\ (ms)^{-1}$
k_{23}	$0.120\ (ms)^{-1}$
k_{32}	$0.030\ (ms)^{-1}$
k_{24}	$0.00045\ (ms)^{-1}$
k_{42}	$0.0004\ (ms)^{-1}$
k_v^{01}	$0.1\ (ms)^{-1}$
k_v^{10}	$0.1\ (ms)^{-1}$

TABLE 6 Binding and Unbinding Transition Rates to Binding Sites Ca-I, Ca-II, and IP3

Rate	Description	Value
k_{12}^{I}	binding rate to Ca-I	$2.0 \times 10^{-4}(ms)^{-1}(\mu M)^{-1}$
k_{21}^{I}	binding off rate to Ca-I	$2.0 \times 10^{-3}(ms)^{-1}$
k_{12}^{II}	binding rate to Ca-II	$2.0 \times 10^{-4}(ms)^{-1}(\mu M)^{-1}$
k_{21}^{II}	binding off rate to Ca-II	$2.0 \times 10^{-3}\ (ms)^{-1}$
k_{12}^{IP3}	binding rate to IP3 site	$1.0 \times 10^{-2}(ms)^{-1}(\mu M)^{-1}$
k_{21}^{IP3}	binding off rate to IP3 site	$5.0 \times 10^{-4}\ (ms)^{-1}$

To account for the interface energies due to ligand binding, we first note that P_o is highly sensitive to both Ca and IP3 concentration in the physiological range. In particular, in the presence of $10\mu M$ IP3, the channel can inactivate from $P_o \sim 0.7$ at $[Ca] \sim 1\mu M$ to $P_o \sim 0.2$ at $[Ca] \sim 100\mu M$. This outcome indicates that, when Ca binds to Ca-I or Ca-II, it can lead to significant energy shifts in the system. This strong dependence on ligand binding suggests that the interface energies induced by Ca binding are large compared to the typical interface energy in the absence of ligand binding. Indeed, we note from the H-bond analysis in Table 1 that many more H-bonds are present at the inter-subunit interface when Ca-I is bound in the closed state than when it is absent in the open state. In this study, we find that a binding energy of $\beta\epsilon_I = -0.75$ gives a good fit for Ca-induced inactivation at large Ca. Now, given that the role of Ca-II is not well established, we will at first assume for simplicity that this site has the same binding energy as Ca-I. Finally, we note that, according to the data of Ionescu et al. (25), P_o is highly sensitive to $[IP3]$. In particular, they found that, at a fixed Ca concentration of $1\mu M$, the open probability can decrease from $P_o \sim 0.6$ to $P_o \sim 0$ as the IP3 concentration is reduced from just $0.1\mu M$ to $0.01\mu M$. To model this sensitive dependence on IP3 concentration, we also found it necessary to make the magnitude of the IP3 binding large relative to the typical interaction strengths between domains. To fit the experimental data, it was necessary to take $\beta\epsilon_{IP3} = -1.5$, which ensured a strong dependence on IP3 concentration, and also that all 4 IP3-binding sites are likely occupied when the IP3 concentration is raised above threshold. This result is consistent with more recent experimental data indicating that all IP3-binding sites need to be occupied in order for the channel to open (15). In Table 7, we show all interface energies that are used in this model. In Fig. 5 *A–C*, we show the experimental and model fits for P_o, τ_c, and τ_o as a function of $[Ca]$ at a fixed $[IP3] = 10\mu M$. Here, we note that the P_o displays the characteristic

Please cite this article in press as: Greene and Shiferaw, A structure-based computational model of IP_3R1 incorporating Ca and IP3 regulation, Biophysical Journal (2024), https://doi.org/10.1016/j.bpj.2024.04.014

TABLE 7 Interface Energies at Ligand-binding Sites

Binding Site	Energy	Value
Ca-I	$\beta\epsilon_I$	-0.75
IP3	$\beta\epsilon_{IP3}$	-1.5
Ca-II	$\beta\epsilon_{II}$	-0.75

bell-shaped dependence on $[Ca]$. This nonmonotonic relationship is also evident in the behavior of both τ_o and τ_c, which is expected since $P_o = \tau_o/(\tau_o + \tau_c)$. The experimental data suggest that this nonmonotonic dependency stems mainly from the strong dependence of τ_c on $[Ca]$. However, it is important to mention that these measurements are noisy and serve primarily as a guide for model fitting rather than for definitive conclusions. In Fig. 5 *D*, we show P_o as the IP3 concentration is varied over the experimental range. These results indicate that our coarse-grained model architecture is sufficient to reproduce the experimentally measured channel properties.

Modal gating

Experimental measurements of the IP_3R current reveal that the channel exhibits three distinct modes of gating behavior (27). In this section, we will examine how our coarse-grained model can be used to explore this channel property. As a starting point, we build on the work of Bicknell et al. (16), who showed that three or four subunits must be in the open state in order for the channel to exhibit modal gating properties. Additionally, they showed that each subunit must have the capacity to transition to a sequestered state independently of Ca and IP3 binding. In our coarse-grained model, the three gating modes are as follows. 1) H mode: all four subunits are in state 2 or 3. In this case, the channel exhibits a fast-bursting mode that is driven by the rapid transitions between state 2 and 3. 2) I mode: three subunits are in state 2 or 3, and one subunit in state 4. In this case, the timescale of the bursting mode will be determined by the substantially slower transitions between state 2 and 4. 3) L mode: two or more subunits are in state 4. In this case, the channel remains closed. In Fig. 6 *A*, we show a typical current trace of the state of the pore, which is open (O) when three or more subunits are in state 3 and closed otherwise. Indeed, the current exhibits three gating modes, which consist of two distinct modes of bursting activity separated by long times of quiescence. Indeed, if we keep track of the number of subunits in the sequestered state, which we denote by n_s, we see that the long-shut time occurs in mode L ($n_s \geq 2$), and that the bursting modes can be separated into two distinct modes characterized by a fast-bursting mode where $n_s = 0$ and a slower bursting mode with $n_s = 1$. To understand how the channel open probability is determined by the mode transitions, in Fig. 6 *B* we plot the within-mode open probability P_o^M, which is defined as the fraction of time spent in the open state during a particular mode. In Fig. 6 *C*, we also plot π^M, which is the fraction of time spent within each mode. These results are consistent with the experimental data on modal gating, which show that the Ca dependence of the open probability is largely dictated by the time spent in each mode rather than the within-mode probability (27). This is a key feature of modal gating, and it is fully reproduced by our coarse-grained model.

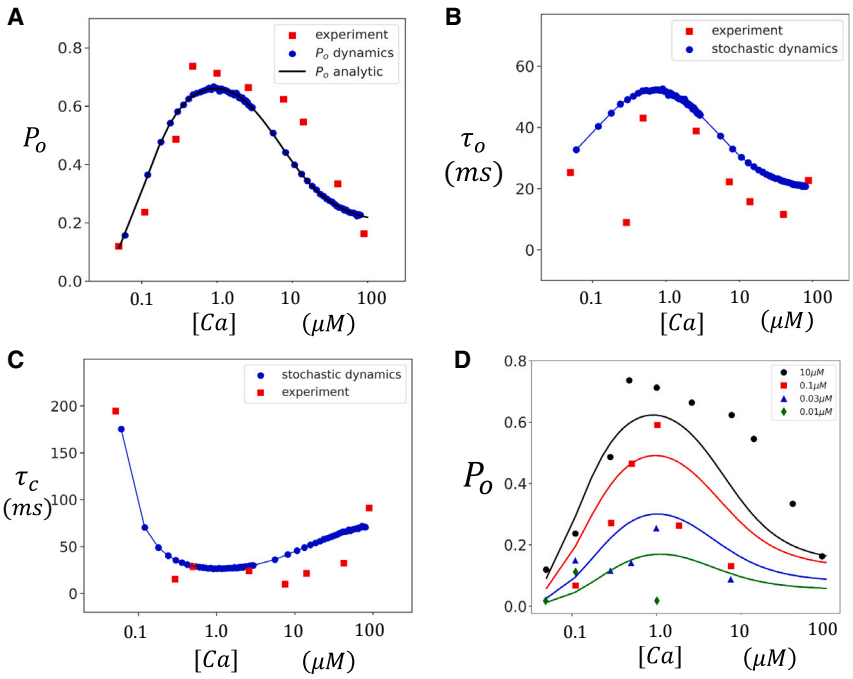

FIGURE 5 Fitting the coarse-grained model with experiments. (*A*) The open probability P_o as a function of $[Ca]$. Experimental data (*red squares*) are shown and model fit with stochastic dynamics (*blue circles*), and equilibrium P_o computed using Eq. 39. The IP3 concentration is fixed at $[IP3] = 10\mu M$. Experimental data are taken from Ionescu et al. (25). (*B*) Mean open time τ_o as a function of $[Ca]$. (*C*) Mean closed time τ_c as a function of $[Ca]$. (*D*) Open probability as a function of $[Ca]$ for a range of IP3 concentrations. To see this figure in color, go online.

Please cite this article in press as: Greene and Shiferaw, A structure-based computational model of IP_3R1 incorporating Ca and IP3 regulation, Biophysical Journal (2024), https://doi.org/10.1016/j.bpj.2024.04.014

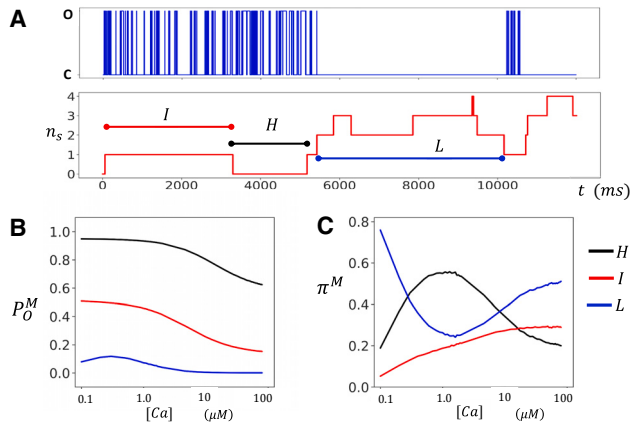

FIGURE 6 Demonstration of modal gating. (*A*) Current trace with $[Ca] = 1\mu M$ and $[IP3] = 10\mu M$. The current transitions between three distinct bursting modes: the fast-burst model (H), the slow-bursting mode (I), and the shut state (L) are indicated in the plot. These modes correspond to $n_s = 0, n_s = 1$, and $n_s = 2$, respectively, where n_s denotes the number of subunits in the sequestered state $s_i = 4$. (*B*) The within-mode open probability P_o^M. (*C*) The fraction of total time π^M spent within each mode. To see this figure in color, go online.

The role of the Ca-II-binding site

An important feature of our coarse-grained model is that it accounts for the spatial relationship between the Ca-I-, Ca-II-, and IP3-binding sites. A key architectural feature of these three binding sites is that they all regulate the interface between $\beta TF2$ and neighboring domains. By taking this structure into account, our model can be used to understand how these binding sites interact to modulate the channel open probability. As a starting point, we will first consider our previously described model of Ca-II in which this site served as a channel inactivator. In that case, Ca binding to Ca-II stabilized the conformation where $\beta TF1$ and $\beta TF2$ were in the states $u_i = 0$ and $v_i = 0$, respectively, which favored channel closure. However, since the binding kinetics of Ca-II is not known, we assumed that the kinetic parameters were identical to Ca-I. To relax this assumption, we will consider a forward-binding rate of the form $k_+^{II} = \alpha\, k_+^I$, where α is a multiplicative constant. We will then vary this parameter to evaluate how the P_o depends on the relative binding rates for Ca-I and Ca-II. In Fig. 7 *A*, we plot the channel P_o as a function of the multiplicative factor α. Here, the case $\alpha = 1$ corresponds to the baseline case where both Ca-I and Ca-II have the same Ca-binding rate. Now, in the case where Ca does not bind to Ca-II ($\alpha = 0$, red line) we see that Ca-induced inactivation of the channel is reduced at high Ca concentrations. In the case where Ca binding to Ca-II is faster than binding to Ca-I ($\alpha = 5$, blue line), we find that Ca inactivation is enhanced. These results indicate that, if Ca-II is an inactivation site, then both Ca-binding sites serve complementary roles to inactivate the channel at high Ca.

To explore the case where Ca-II serves as a channel activator, we choose the binding energy ϵ_{II} to stabilize the conformation where $\beta TF2$ is in the state $v_i = 1$ and $\beta TF1$ is in the state $u_i = 0$. In this way, stronger Ca binding to Ca-II will favor a larger channel P_o since it will become more energetically favorable for $\beta TF2$ to reside in the state $v_i = 1$. To explore this case over a broad range of parameters, we will again take $k_+^{II} = \alpha\, k_+^I$ to vary the binding rate of Ca-II relative to Ca-I. In Fig. 7 *B*, we plot the case where $\alpha = 0$ (black line), $\alpha = 0.1$ (red line), and $\alpha = 1.0$ (blue line). These results indicate that, when the forward rate of Ca-II is increased from zero, even by just 10% of the Ca-I reaction rate, the channel P_o loses its typical bell-shaped curve. The reason for this behavior is that, even for a small binding rate k_+^{II}, at high enough Ca concentrations where $[Ca] > k_-^{II}/k_+^{II}$, the activating effect of Ca-II will balance the inactivating effect of Ca-I. Thus, if Ca-II is a channel activator, the channel P_o is unlikely to exhibit the bell-shaped open probability seen experimentally (25). Therefore, our results suggest that Ca-II is likely to be an inactivating site. If this is not the case, then the binding rate at this site should be extremely weak relative to Ca-I, which would render this site irrelevant to the channel open probability in the physiological range of Ca. Overall, our results suggest that the characteristic bell-shaped open probability and the signaling architecture of the βTF ring necessitate that Ca-II is an inactivation site.

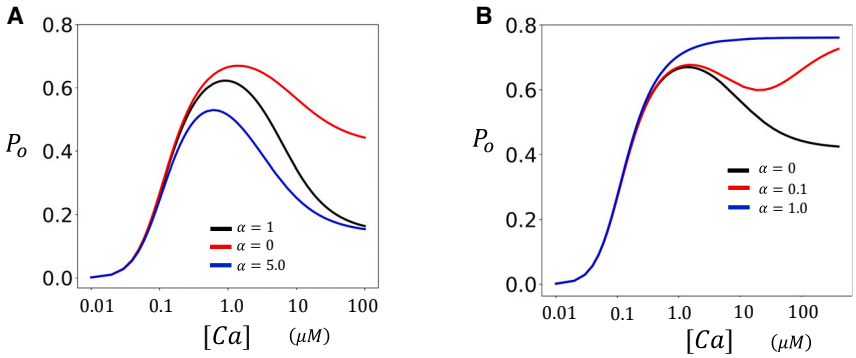

FIGURE 7 The dependence of the open probability P_o on kinetic parameters of the Ca-I- and Ca-II-binding sites. (*A*) P_o vs. $[Ca]$. Here, the Ca-binding rates to Ca-II have the form $k_+^{II} = \alpha\, k_+^I$. In this case, Ca binding to Ca-II stabilizes the closed state of the channel. (*B*) The case where Ca binding stabilizes the open state of the channel. To see this figure in color, go online.

Please cite this article in press as: Greene and Shiferaw, A structure-based computational model of IP_3R1 incorporating Ca and IP3 regulation, Biophysical Journal (2024), https://doi.org/10.1016/j.bpj.2024.04.014

Cooperativity and domain-domain interactions

Our computational framework can be used to explore how the interaction between domains shapes the open probability of the channel. In a recent study, we analyzed the role of subunit-subunit interactions in RyR2 and showed that these interactions were crucial for channel cooperativity (31). In this study, we analyze how specific domain-domain interactions in IP_3R1 influence the shape of the channel open probability. As a starting point, we first consider the role of the interaction between neighboring s-regions, which is controlled by the interface energy $E'_{ss}(s_i, s_{i+1})$ (Table 2). Recall, that our H-bond analysis, shown in Table 1, identified key contacts that link the s-region in adjacent subunits, so it is expected that these interactions will drive cooperativity of the channel. To explore a range of interaction strengths, we will scale the interface energy by a factor λ, so that $E'_{ss}(s_i, s_{i+1}) \rightarrow \lambda\, E'_{ss}(s_i, s_{i+1})$. In Fig. 8 *A*, we plot P_o for the case where there are no interactions between the s-regions ($\lambda = 0$, red line) to the case where there are strong interactions ($\lambda = 5$, blue line), and where $\lambda = 1$ (black line) corresponds to our baseline model parameter that was used to fit the experimental data in Fig. 5. Our results show that the interaction energy between adjacent s-regions controls the nonlinear response of P_o to $[Ca]$ at both the activation and inactivation threshold. In particular, at Ca concentrations where the channel is activated ($[Ca] \sim 0.1\mu M$), increasing λ sharpens the nonlinear increase of P_o as a function of $[Ca]$. At low Ca concentrations when the channel is closed, the interaction between subunits will control the stability of the closed state. In Fig. 8 *B*, we plot the mean closed time τ_c as a function of Ca at concentrations in the range $0.001 - 0.1\mu M$. Here, we find that τ_c increases by more than an order of magnitude as the subunit-subunit interaction is scaled from $\lambda = 0$ to $\lambda = 5$. Thus, the interactions between adjacent subunits have a pronounced effect on the stability of the closed state of the channel at low Ca. Similarly, at large Ca concentrations where inactivation of the channel occurs, we find that the P_o decreases more rapidly as a function of $[Ca]$ when the interaction strength λ is increased. These results indicate that the interface energy between adjacent s-regions improves the signaling fidelity of the channel to changes in Ca concentration. In Fig. 8 *C*, we have also varied the interaction strength of the coupling between the s-region of subunit i and $\beta TF2$ in subunit $i - 1$. This interface energy is determined by the term $E'_{sv}(\tilde{s}_i, v_{i-1})$, which we have scaled by a factor λ to explore a range of interaction strengths. Here, we observe that an increase in the coupling strength again results in an enhanced nonlinear threshold dependence on Ca concentration. However, in this case, the impact of coupling strength is more pronounced on the inactivation of the channel at high Ca concentration. This is because $\beta TF2$ mediates the inactivation of the channel at high Ca concentrations. As a result, the presence of cooperativity significantly amplifies these effects at these high concentration ranges. Overall, these results indicate that variations in

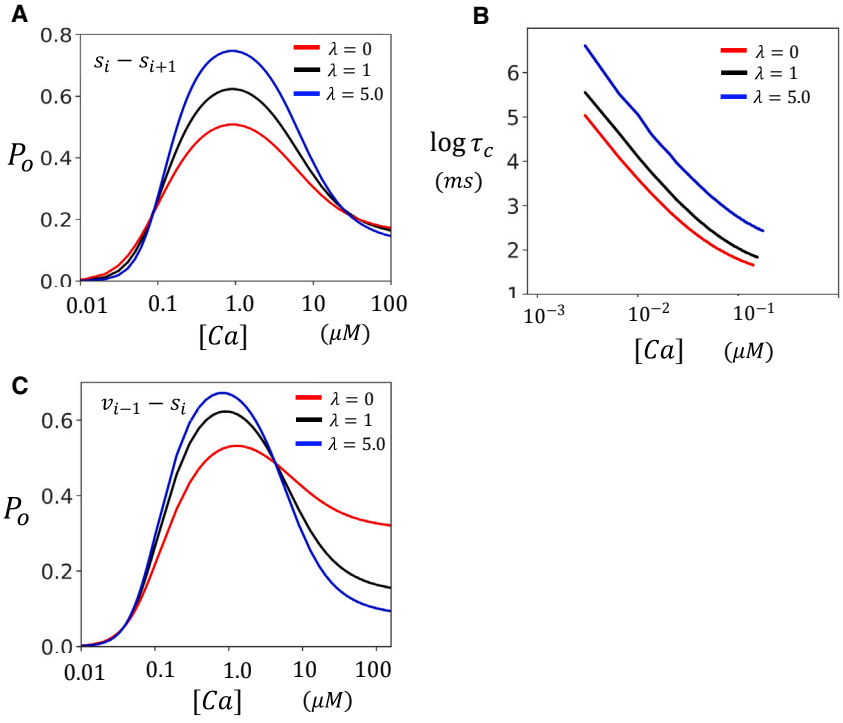

FIGURE 8 Dependence of open probability on domain-domain interactions. (*A*) Open probability vs. $[Ca]$ for a range of interface energies between the s-region of subunit i and the neighboring subunit at $i + 1$. The interface energy is scaled according to $E'_{ss}(\tilde{s}_i, \tilde{s}_{i+1}) \rightarrow \lambda E'_{ss}(\tilde{s}_i, \tilde{s}_{i+1})$. (*B*) The mean closed time τ_c vs. $[Ca]$ for the indicated range of interface energies. (*C*) Dependence of open probability on Ca for a range of interaction strengths between $\beta TF2$ on subunit $i - 1$ and the s-region of subunit i. Interaction energy is scaled according to $E'_{sv}(\tilde{s}_i, v_{i-1}) \rightarrow \lambda E'_{sv}(\tilde{s}_i, v_{i-1})$. To see this figure in color, go online.

Please cite this article in press as: Greene and Shiferaw, A structure-based computational model of IP_3R1 incorporating Ca and IP3 regulation, Biophysical Journal (2024), https://doi.org/10.1016/j.bpj.2024.04.014

the interaction strengths between different channel domains and regions can lead to a spectrum of functional outcomes.

DISCUSSION

Recent advances in cryo-EM have provided new insights on the crystal structure of IP_3R at an unprecedented level of detail (10–14,32). These studies suggest that the channel function is determined by the movement of large structural domains that control the opening of the channel pore. Additionally, these structures indicate that the motion of these domains is regulated by ligand-binding sites situated at the interface between domains on the same subunit and at the interface between neighboring subunits. Thus, the architecture of IP_3R is highly cooperative by construction, and this likely plays a crucial role in channel function. In this study, we have developed a coarse-grained model based on the spatial architecture of IP_3R1 that was recently revealed in the cryo-EM structures provided by Fan et al. (11). This model accounts for energetic interactions between domains and ligand regulation of these interactions, and it satisfies detailed balance at equilibrium. To our knowledge, this is the first computational model that accounts for cooperative intra- and inter-subunit interactions within the full IP_3R tetramer in a thermodynamically consistent manner. Previous Markovian models of IP_3R did not include cooperativity between subunits since the architecture of domain interactions was largely unknown (16). Using this model, we have investigated how the open probability of the channel depends on cooperative interactions between domains. Our main finding is that the nonlinear switch-like dependence of the open probability on the Ca concentration is highly sensitive to domain-domain interactions. Specifically, we find that the stability of the closed state is highly sensitive to domain-domain interactions between neighboring subunits. This result implies that a disruption of these interactions will lead to a leaky IP_3R1 channel at low Ca concentrations. Also, we find that the decrease of open probability at high Ca is also highly sensitive to interactions between subunits. In this case, weakened cooperative interactions reduce the regulatory effect of the βTF ring, and this will prevent the channel from closing. Thus, reduced cooperativity between subunits will make the channel leakier by allowing fluctuations to the open state to occur at low Ca and also by preventing the channel from closing at high Ca concentration levels. This is an important finding since leaky Ca channels have been linked to a wide range of disease states (33–36). The reason behind this is that a leaky channel can lead to an elevated steady state of cytosolic Ca concentration, which can lead to impaired recovery of the Ca signaling process. Thus, since Ca plays a crucial role in regulating numerous cellular activities, an abnormal increase in Ca has the potential to disrupt various processes, including structural remodeling and protein synthesis (37–40). Also, a variety of cardiac abnormalities, such as heart failure, have been traced to leaky ryanodine receptor type 2 (RyR2) channels, which share many structural features with IP_3R (23,31,41,42). In this case, we also expect that impaired domain-domain interactions will lead to leaky RyR2 channels, which will lead to a disturbance of Ca homeostasis in cardiac myocytes. Our study suggests that these disease-causing abnormalities can be traced to a disruption in the interactions between neighboring subunits of the channel.

The cryo-EM structures provided by Fan et al. of the open and closed IP_3R1 channel reveal the architecture of ligand regulation on the cytosolic side of the channel. The key insight from these structural studies is that the βTF ring plays a central role in Ca and IP3 regulation. In particular, both Ca-binding sites and the IP3-binding site appear in close proximity to $\beta TF2$. Specifically, IP3 binding regulates the interaction between the $\beta TF2$ domain and the domains that directly regulate the pore. Also, the positioning of Ca ions in the cryo-EM structures suggest that Ca-I regulates the interaction between $\beta TF2$ and $\beta TF1$ on an adjacent subunit, whereas Ca-II regulates the interaction between $\beta TF2$ and $\beta TF1$ on the same subunit. The logical structure of this network of interactions suggests that $\beta TF1$ plays an inactivating role, since stronger binding to this domain, at least via Ca-I, reduces the channel P_o. On the other hand, $\beta TF2$ likely functions as a channel activator since stronger binding to this domain, mediated by IP3 binding, is necessary for the channel to open. However, the role of Ca-II is less clear, and, in this study, we have explored the case where this site is both an activator or an inactivator. In the case where Ca-II serves as an inactivating binding site, the effect is simply to accentuate the effect of Ca-induced inactivation as the decrease of P_o, which is observed at high Ca, is more pronounced. In this case Ca-I and Ca-II will serve synergistic roles to inactivate the channel at large Ca. Alternatively, if Ca-II serves the role as an activator, then we find that the inactivation of the channel at large Ca is compromised. In this case, the system cannot exhibit a bell-shaped dependence on Ca since the Ca-I-binding site will saturate and eventually, for high enough Ca, the activating effect of Ca-II will manifest. In this case, our study predicts that the P_o of the channel will not exhibit a bell-shaped dependence on Ca. Since this effect is not observed experimentally, Ca-II is unlikely to serve as an activating site. Therefore, our coarse-grained model suggests that Ca-II likely serves a complementary role to Ca-I, and the signaling architecture is inconsistent with Ca-II serving as a channel-activating site.

Our coarse-grained model provides a clear interpretation of allostery in the context of IP_3R1. In this picture, allosteric regulation of the channel is due to ligand binding, which strengthens the interactions between domains. Consequently, allostery modulates the cooperativity between

Please cite this article in press as: Greene and Shiferaw, A structure-based computational model of IP_3R1 incorporating Ca and IP3 regulation, Biophysical Journal (2024), https://doi.org/10.1016/j.bpj.2024.04.014

domains within each subunit and between the four subunits that constitute the channel. Also, the nonlinear relationship between channel open probability and ligand concentration is due to competing domain-domain interactions, which are regulated by distinct ligand-binding sites. This interpretation is consistent with several studies seeking to explain the structural and energetic basis of allostery (43). However, there are several limitations that should be considered when interpreting the results of this study. In particular, although our model is derived from the channel structure unveiled by cryo-EM, the resolution is not adequate to quantitatively assess the interaction strengths between the domains of IP_3R. Thus, the current level of structural detail is not sufficient to model the structural dynamics quantitatively. To overcome this challenge, we have resorted to counting bonds as a method to estimate the presence of cooperative interactions. Given this limitation, our modeling approach does have predictive value since the architecture of the system provides important constraints on the ligand dependence of the open probability. Thus, we deduce the role of the Ca-II-binding site based on basic principles derived from our simplified model. In the future, this approach to model building can be significantly improved with access to more refined structural data. This improvement will lead to a more precise understanding of IP3R dynamics and the relationship between its structure and function. Also, the computational model is highly dependent on the details of the channel architecture of IP_3R1 measured by Fan et al. (11) This channel architecture is quite complex, and many additional regulatory aspects of the channel, including ATP and luminal Ca interaction sites, are not captured in our present coarse graining approach. We must also emphasize that our regulatory model is based on the structure of IP_3R1. A recently released cryo-EM structure of IP_3R3 by Paknejad et al. (32) revealed a completely different regulation scheme than that of IP_3R1. The IP_3R3 structure had a Ca-III-binding site and only one additional Ca-binding site, which was linked to channel inactivation. Structurally, the inactivation Ca-binding site on IP_3R3 was not located near the $\beta TF1$ and $\beta TF2$ interface as it was in IP3R1, but was instead located on the outer periphery of the channel, at the interface between ARM2 and the central linker domain (32,44). The inactivation mechanism proposed by Paknejad et al. (32) is also very different, as the closed structure in IP_3R3 involves an opening of the βTF ring. This was very much the opposite of the closing of the βTF ring that was indicated by an increase in H-bonds at the inter-subunit $\beta TF1$ and $\beta TF2$ interface in the closed IP_3R1 structure. Nevertheless, the model framework that we have developed here can readily be extended to include additional regulatory ligands or different channel types with different regulatory strategies. Such extensions of this model framework will be necessary as additional structural details related to IP_3R channel regulation become available in future studies.

AUTHOR CONTRIBUTIONS

D.G. and Y.S. designed and performed research, contributed analytic tools, analyzed data, and wrote the paper.

ACKNOWLEDGMENTS

This work was supported by the National Heart, Lung, and Blood Institute grant R16 GM153647-01.

DECLARATION OF INTERESTS

The authors declare no competing interests.

REFERENCES

1. Mikoshiba, K. 2007. IP3 receptor/Ca2+ channel: from discovery to new signaling concepts. *J. Neurochem.* 102:1426–1446.
2. Bootman, M. D., M. J. Berridge, and H. L. Roderick. 2002. Calcium signalling: more messengers, more channels, more complexity. *Curr. Biol.* 12:R563–R565.
3. Berridge, M. J. 2009. Inositol trisphosphate and calcium signalling mechanisms. *Biochim. Biophys. Acta.* 1793:933–940.
4. Roderick, H. L., and M. D. Bootman. 2007. Pacemaking, arrhythmias, inotropy and hypertrophy: the many possible facets of IP3 signalling in cardiac myocytes. *J. Physiol.* 581:883–884.
5. Bers, D. 2001. Excitation-contraction Coupling and Cardiac Contractile Force. Springer Science & Business Media.
6. Hund, T. J., A. P. Ziman, …, P. J. Mohler. 2008. The cardiac IP3 receptor: Uncovering the role of "the other" calcium release channel. *J. Mol. Cell. Cardiol.* 45:159–161.
7. Ju, Y.-K., J. Liu, …, D. G. Allen. 2011. Distribution and Functional Role of Inositol 1, 4, 5-tris phosphate Receptors in Mouse Sinoatrial Node. *Circ. Res.* 109:848–857.
8. Dridi, H., G. Santulli, …, A. R. Marks. 2022. IP3 receptor orchestrates maladaptive vascular responses in heart failure. *J. Clin. Invest.* 132, e152859.
9. Woll, K. A., and F. Van Petegem. 2022. Calcium-release channels: Structure and function of IP3 receptors and ryanodine receptors. *Physiol. Rev.* 102:209–268.
10. Schmitz, E. A., H. Takahashi, and E. Karakas. 2022. Structural basis for activation and gating of IP3 receptors. *Nat. Commun.* 13:1408.
11. Fan, G., M. R. Baker, …, I. I. Serysheva. 2022. Conformational motions and ligand-binding underlying gating and regulation in IP3R channel. *Nat. Commun.* 13:6942.
12. Paknejad, N., and R. K. Hite. 2018. Structural basis for the regulation of inositol trisphosphate receptors by Ca2+ and IP3. *Nat. Struct. Mol. Biol.* 25:660–668.
13. Hamada, K., H. Miyatake, …, K. Mikoshiba. 2017. IP_3-mediated gating mechanism of the IP_3 receptor revealed by mutagenesis and X-ray crystallography. *Proc. Natl. Acad. Sci. USA.* 114:4661–4666.
14. Bosanac, I., J.-R. Alattia, …, M. Ikura. 2002. Structure of the inositol 1, 4, 5-trisphosphate receptor binding core in complex with its ligand. *Nature.* 420:696–700.
15. Alzayady, K. J., L. Wang, …, D. I. Yule. 2016. Defining the stoichiometry of inositol 1, 4, 5-trisphosphate binding required to initiate Ca2+ release. *Sci. Signal.* 9:ra35.
16. Bicknell, B. A., and G. J. Goodhill. 2016. Emergence of ion channel modal gating from independent subunit kinetics. *Proc. Natl. Acad. Sci. USA.* 113:E5288–E5297.
17. Shuai, J., J. E. Pearson, …, I. Parker. 2007. A kinetic model of single and clustered IP3 receptors in the absence of Ca2+ feedback. *Biophys. J.* 93:1151–1162.

18. Siekmann, I., P. Cao, …, E. J. Crampin. 2019. Data-driven modelling of the inositol trisphosphate receptor (IP3R) and its role in calcium-induced calcium release (CICR). *In* Computational Glioscience. M. De Pittà and H. Berry, eds Springer, pp. 39–68.
19. Siekmann, I., L. E. Wagner, …, J. Sneyd. 2012. A Park/Drive Model for the Inositol-Trisphosphate Receptor (IPR). *Biophys. J.* 102:110a.
20. Ullah, G., D. O. D. Mak, and J. E. Pearson. 2012. A data-driven model of a modal gated ion channel: The inositol 1, 4, 5-trisphosphate receptor in insect Sf9 cells. *J. Gen. Physiol.* 140:159–173.
21. Marzen, S., H. G. Garcia, and R. Phillips. 2013. Statistical mechanics of monod–wyman–changeux (mwc) models. *J. Mol. Biol.* 425:1433–1460.
22. Einav, T., and R. Phillips. 2017. Monod-Wyman-Changeux analysis of Ligand-Gated ion channel mutants. *J. Phys. Chem. B.* 121:3813–3824.
23. Greene, D., M. Barton, …, Y. Shiferaw. 2022. Molecular dynamics simulations of the cardiac ryanodine receptor type 2 (RyR2) gating mechanism. *J. Phys. Chem. B.* 126:9790–9809.
24. Phillips, R. 2020. The Molecular Switch: Signaling and Allostery. Princeton University Press.
25. Ionescu, L., K. H. Cheung, …, J. K. Foskett. 2006. Graded recruitment and inactivation of single InsP3 receptor Ca2+-release channels: implications for quartal Ca2+ release. *J. Physiol.* 573:645–662.
26. Goddard, T. D., C. C. Huang, …, T. E. Ferrin. 2018. UCSF ChimeraX: Meeting modern challenges in visualization and analysis. *Protein Sci.* 27:14–25.
27. Ionescu, L., C. White, …, D.-O. D. Mak. 2007. Mode switching is the major mechanism of ligand regulation of InsP3 receptor calcium release channels. *J. Gen. Physiol.* 130:631–645.
28. Arige, V., L. E. Terry, …, D. I. Yule. 2022. Functional determination of calcium-binding sites required for the activation of inositol 1, 4, 5-trisphosphate receptors. *Proc. Natl. Acad. Sci. USA.* 119, e2209267119.
29. Salinas, R. K., L. Bruschweiler-Li, …, R. Brüschweiler. 2011. Ca2+ binding alters the interdomain flexibility between the two cytoplasmic calcium-binding domains in the Na+/Ca2+ exchanger. *J. Biol. Chem.* 286:32123–32131.
30. Gillespie, D. T. 2007. Stochastic simulation of chemical kinetics. *Annu. Rev. Phys. Chem.* 58:35–55.
31. Greene, D., T. Luchko, and Y. Shiferaw. 2023. The role of subunit cooperativity on ryanodine receptor 2 calcium signaling. *Biophys. J.* 122:215–229.
32. Paknejad, N., V. Sapuru, and R. K. Hite. 2023. Structural titration reveals Ca2+-dependent conformational landscape of the IP3 receptor. *Nat. Commun.* 14:6897.
33. Dridi, H., A. Kushnir, …, A. R. Marks. 2020. Intracellular calcium leak in heart failure and atrial fibrillation: a unifying mechanism and therapeutic target. *Nat. Rev. Cardiol.* 17:732–747.
34. Bers, D. M. 2014. Cardiac sarcoplasmic reticulum calcium leak: basis and roles in cardiac dysfunction. *Annu. Rev. Physiol.* 76:107–127.
35. Lehnart, S. E., M. Mongillo, …, A. R. Marks. 2008. Leaky Ca 2+ release channel/ryanodine receptor 2 causes seizures and sudden cardiac death in mice. *J. Clin. Invest.* 118:2230–2245.
36. Wehrens, X. H. T., S. E. Lehnart, and A. R. Marks. 2005. Intracellular calcium release and cardiac disease. *Annu. Rev. Physiol.* 67:69–98.
37. Liu, Z., J. E. Finet, …, J. K. Donahue. 2019. Calcium/calmodulin-dependent protein kinase II causes atrial structural remodeling associated with atrial fibrillation and heart failure. *Heart Rhythm.* 16:1080–1088.
38. Lou, Q., A. Janardhan, and I. R. Efimov. 2012. Remodeling of calcium handling in human heart failure. *Adv. Exp. Med. Biol.* 740:1145–1174.
39. Rosen, L. B., D. D. Ginty, and M. E. Greenberg. 1995. Calcium regulation of gene expression. *Adv. Sec. Messenger Phosphoprotein. Res.* 30:225–253.
40. Brostrom, C. O., and M. A. Brostrom. 1990. Calcium-dependent regulation of protein synthesis in intact mammalian cells. *Annu. Rev. Physiol.* 52:577–590.
41. Belevych, A. E., P. B. Radwański, …, S. Györke. 2013. 'Ryanopathy': causes and manifestations of RyR2 dysfunction in heart failure. *Cardiovasc. Res.* 98:240–247.
42. Marx, S. O., and A. R. Marks. 2013. Dysfunctional ryanodine receptors in the heart: new insights into complex cardiovascular diseases. *J. Mol. Cell. Cardiol.* 58:225–231.
43. Hilser, V. J., J. O. Wrabl, and H. N. Motlagh. 2012. Structural and energetic basis of allostery. *Annu. Rev. Biophys.* 41:585–609.
44. Baker, M. R., G. Fan, …, I. I. Serysheva. 2023. Understanding IP3R Channels: from structural underpinnings to ligand-dependent conformational landscape. *Cell Calcium.* 114, 102770.